

# MFIF-GAN: A New Generative Adversarial Network for Multi-Focus Image Fusion

Yicheng Wang, Shuang Xu, Junmin Liu\*, Zixiang Zhao, Chunxia Zhang,  
Jiangshe Zhang

*School of Mathematics and Statistics, Xi'an Jiaotong University*

---

## Abstract

Multi-Focus Image Fusion (MFIF) is a promising image enhancement technique to obtain all-in-focus images meeting visual needs and it is a precondition for other computer vision tasks. One of the research trends of MFIF is to avoid the defocus spread effect (DSE) around the focus/defocus boundary (FDB). In this paper, we propose a network termed MFIF-GAN to attenuate the DSE by generating focus maps in which the foreground region are correctly larger than the corresponding objects. The *Squeeze* and *Excitation* Residual module is employed in the network. By combining the prior knowledge of training condition, this network is trained on a synthetic dataset based on an  $\alpha$ -matte model. In addition, the reconstruction and gradient regularization terms are combined in the loss functions to enhance the boundary details and improve the quality of fused images. Extensive experiments demonstrate that the MFIF-GAN outperforms several state-of-the-art (SOTA) methods in visual perception, quantitative analysis as well as efficiency. Moreover, the edge diffusion and contraction module is firstly proposed to verify that focus maps generated by our method are accurate at the pixel level.

**Keywords:** multi-focus image fusion, defocus spread effect, generative adversarial network, deep learning.

---



---

\*Corresponding author

Email address: junminliu@mail.xjtu.edu.cn (Junmin Liu)

## 1. Introduction

In the field of digital photography, the limited depth-of-field (DOF) leads to multiple images focused at different regions in the same scene and the defocus spread effect (DSE) [1]. As an image enhancement technique, Multi-Focus Image Fusion (MFIF) has been studied to fuse multi-focus images, as shown in Fig.1(a) and 1(b), so that the fusion result shown in Fig.1(c) retains the clear information of the sources. It is a pre-condition for various kinds of computer vision (CV) tasks, such as localization, object detection, recognition and segmentation [2, 3].

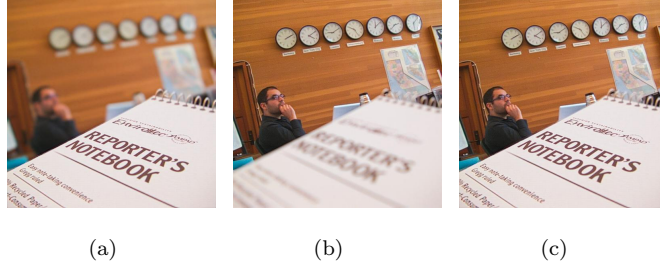


Figure 1: The source of MFIF images and desired fusion result

The past few decades have witnessed the rapid development of abundant MFIF algorithms. Generally, the classic MFIF algorithms can be categorized into two groups: transform domain and spatial domain methods[4]. The idea of the former is to transform the images from the original image space into an abstract feature space so that the active level of source images can be detected and measured easily. Then a desired image is reconstructed from the feature space into the image space after merging the active feature according to a certain fusion strategy[5]. The typical transform domain methods include the non-subsampled contourlet transform (NSCT) [6, 7], the sparse representation (SR) [8, 9] and the combined NSCT-SR [10]. The drawback is that these algorithms often produce unrealistic results, even in the areas far away from the focus/defocus boundary (FDB) [1].

Based on the assumption that each pixel, block or region is either focused or defocused [11], the spatial domain methods can be classified into three cate-

gories: pixel-based, block-based and region-based algorithms which discriminate the focused condition at the pixel, block or region level respectively. However, the pixel-based methods such as [12] suffer from misregistration [13]. The block-based techniques such as [14] [15] generally are sensitive to the block-size [16]. And the efficiency and performance of the region-based algorithms such as [17] [18] are usually influenced by the region segmentation procedures.

In the past few years, Deep Learning (DL) has aroused researchers widespread interests for its surprising effectiveness in CV applications. Liu et al. [19] made the first attempt to apply convolutional neural networks (CNNs) to MFIF. In their work, the siamese architecture was used to extract the feature of the focused and defocused regions. Guo et al. [20] proposed a fully convolutional network for focus detection. And a cascaded boundary aware convolutional network [1] was introduced to achieve clear results around the FDB. Inspired by the DL tools and region based methods, deep semantic segmentation and edge detection algorithms are employed in MFIF to capture clear focus maps [21, 22].



Figure 2:  $I_A$  without DSE and  $I_B$  suffering from DSE

However, apart from [1, 5], few of previous works take the DSE into account. So at present, in order to get fusion images with higher quality, one of the important research trends of MFIF is to avoid this spread effect. Actually, the DSE describes a common phenomenon that the FDB sometimes is a ribbon region with the uncertain width instead of a clear curve. More precisely, when the foreground is in focus, the blurred background object will not influence

the clear foreground region, that is, the FDB is clear as displayed in Fig.2(a)  $I_A$ . However, when the foreground is defocused, the blurred foreground will permeate the background. Obviously, the FDB is not a clear line and blurred foreground objects are mildly bigger than itself as shown in Fig.2(b)  $I_B$ .

In this paper, we present a new DL-based MFIF algorithm termed MFIF-GAN to attenuate the DSE by generating focus maps in which the foreground regions are appropriately larger than the corresponding objects. Specifically, the SE-ResNet [23] is exploited as attention mechanism and the reconstruction loss along with gradient penalty are utilized to enhance the boundary details and improve the quality of fused results. In addition, a large-scale training dataset suffering from the DSE is synthesized by applying an  $\alpha$ -matte boundary defocus model [1] to the VOC 2012 dataset [24]. At last, initial focus maps generated by the network are refined by a post-processing algorithm in a computational efficient manner.

A series of experiments are carried out to demonstrate the superiority of our method over the state-of-the-art (SOTA) algorithms qualitatively and quantitatively. In order to verify the rationality of the generated focus maps, we proposed a diffusion and contraction module to expand or shrink the foreground region at the pixel level. In addition, ablation experiments are conducted to study the role of each element in our network.

The contributions of this paper are as follows:

1. A new multi-focus image fusion algorithm named MFIF-GAN with a new structure and well-designed loss functions is proposed.
2. A more realistic dataset with DSE is constructed using an  $\alpha$ -matte model which can be a new benchmark training set for other supervised MFIF algorithms.
3. Training on this new dataset makes the proposed network a better performance qualitatively and quantitatively than several SOTAs. With the computationally lightweight post-processing, the fusion procedure of this algorithm is fastest with respect to the above methods.

4. Generating focus maps with larger foregrounds could be a simple and ingenious solution for further researches to alleviating the DSE. And a diffusion and contraction module is firstly introduced to verify this statement.

The rest of this paper is arranged as follows. In section 2, a briefly review of related works is provided in which the  $\alpha$ -matte model, attention mechanisms and FuseGAN are introduced. Section 3 describes the details of the proposed network. Then, contrast experiments are conducted in section 4 to evaluate all methods qualitatively and quantitatively. The effectiveness of the new solution for attenuating the DSE is also proved by diffusion and contraction experiments. And ablation experiments are conducted in this section. At last, conclusions are drawn in section 5.

## 2. Related Works

### 2.1. $\alpha$ -matte Model for MFIF Datasets

Due to the lack of large scale datasets of multi-focus images, several data generation methods based on public natural image datasets were adopted in many DL-based algorithms [11, 19, 25, 26, 27]. For example, in FuseGAN [11], a multi-focus image dataset was synthesized based on PASCAL VOC 2012 dataset [24]. Fidel et al.[20] and Guo et al.[28] used MS COCO and CIFAR-10 respectively to constructed MFIF training datasets.

However, the DSE is neglected in all datasets above. The unrealistic training data may limit the performance of theses algorithms [1]. Therefore, Ma et al. [1] proposed a novel  $\alpha$ -matte model which provides a insightful point of view to understand the DSE and real world multi-focus images. More details about the generation of training data is discussed in section 4.1.1.

### 2.2. Attention Mechanisms and Squeeze-Excitation Block

Apart from traditional CNNs, some researchers attend to strengthen the representation of networks to focus on salient objects in images for particular

tasks. That is, in MFIF issue, consistent with the procedure of generating a rational focus map characterizing the objects which are in or out of focus.

As an attention mechanism, Hu et al. proposed the SE block [23] consisting of a *squeeze* and a *excitation* operation, which model the interdependencies between the channels of feature maps to recalibrate them. The squeeze module outputs a global distribution of features by aggregating feature maps across spatial dimensions. And using a gating mechanism, the excitation operation produces a collection of weights representing the relationships between the channels. Meanwhile, the SE block could be directly integrated into other networks such as residual [29] and inception [30] networks as an atomic building block. In our work, the combined SE-ResNet module is exploited to extract the implicit features with multi-channels.

### 2.3. FuseGAN for Multi-Focus Images to Focus Map Translation

Inspired by the conditional generative adversarial network [31] for image-to-image translation and the siamese network for extracting features of multi-focus images [19], FuseGAN [11] was proposed for MFIF task, which employed the objective function of LSGAN [32] and exploited the convolutional conditional random fields (ConvCRFs) based technique [33] as a post-processing algorithm. Compared with other spatial domain methods (CNN [19], BF [18] and DSIFT [15]), the focused regions detected by FuseGAN are closer to the ground truth. In our experiments, FuseGAN is regarded as a baseline network.

The disadvantages of FuseGAN are summarized as follows. (1) As it is designed for gray images, the important color information may get lost, that could limit the performance of the method. (2) It should be noted that the distinction between images will be excessively magnified by  $\ell_2$ -norm based adversarial loss used in FuseGAN, which could make the training unstable. (3) As for the additional reconstruction loss function, the coefficient  $\lambda_{rec}$  of the binary cross entropy (BCE) loss is set very large which has no interpretability. And Aritra Ghosh et al. [34] argued that the cross entropy is commonly sensitive to label noise in classification tasks. (4) Last but not least, the ConvCRFs does not work

if all-in-focus images as ground truth are not available, leading to unsatisfactory results in the real application.

### 3. The Proposed Method

Lots of previous MFIF algorithms have achieved good fusion performances, but few works concentrate on the DSE. For example, the unsupervised MFF-GAN [35] which has a well-designed decision block and adaptive content loss function does not analyse the essence of the defocus spreading. In this section, we propose a supervised GAN-based network for the MFIF task, especially for alleviating the DSE. To begin with, we introduce the symbols used in this paper.

The source image  $I_A$  corresponds to the image which has a clear foreground with a blurred background. While another source  $I_B$  suffering from the DSE has a blurred foreground with a clear background. The all-in-focus image denotes as  $I$ . In the synthetic training set, it is regarded as the ground truth. The binary segmentation map  $F$  represents a focus map, where  $F_{ij} = 1$  if  $(i, j)$  pixel is in focus and 0 otherwise. The focus map generated by the network and the one refined by post-processing are denoted by  $\hat{F}$  and  $\hat{F}_{final}$  respectively.

#### 3.1. Architecture of the Network

As a variant of GAN [36], MFIF-GAN also consists of two fundamental modules: a generator and a discriminator. The architecture of our network is shown in Fig.3. The generator in MFIF-GAN is fed with the source color images  $I_A$  and  $I_B$  aiming to generate focus map  $\hat{F}$ . The inputs of the discriminator are the concatenation of  $I_A$ ,  $I_B$  and the (real or generated) focus map. The aim of the generator is to reconstruct focus maps as accurately as possible, while the purpose of the discriminator is to distinguish the generated focus maps from the real ones.

**Generator  $G$ :** The  $G$  includes an encoder, a tensor concatenation module and a decoder. In order to effectively process color images, the encoder is designed as six branches of parallel sub-networks sharing parameters for each channel of source images.

Each sub-network in encoder is composed of three convolutional modules and nine residual blocks. In order to reduce computation burden, the 2nd and 3rd convolutional modules with a stride of 2 down-sample feature maps. Furthermore, inspired by SE-Net [23] as an attention mechanism, each residual block is equipped with a SE block as SE-ResNet to find the interdependencies between the channels of feature maps and extract the most informative components of the images. In every SE-ResNet module, the SE block is attached to the non-identity branch which is a defaulted residual module with two convolutional layers and batch normalization (BatchNorm) [37] to guarantee the squeeze and excitation operations work before addition with the identity branch.

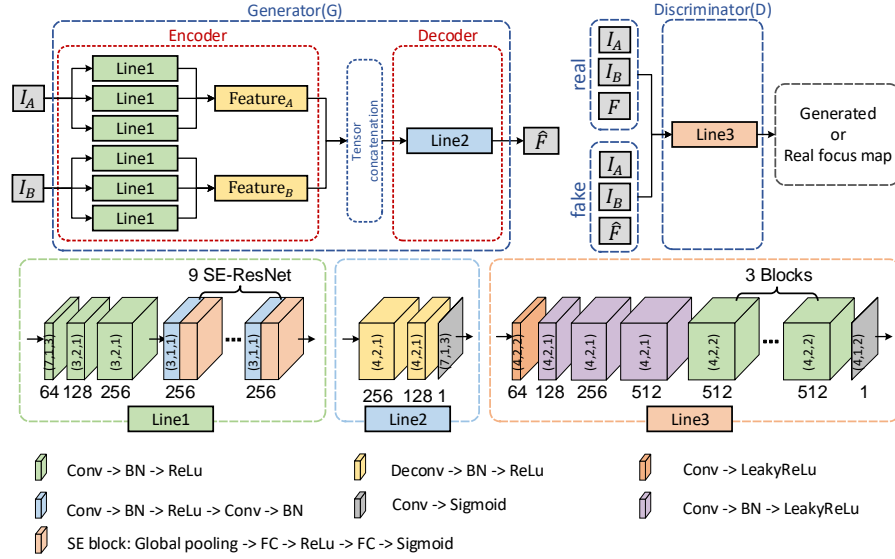


Figure 3: The work flow of the training and the detail architecture of MFIF-GAN. The convolutional layer, transposed convolutional layer, BatchNorm layer, Rectified Linear Unit and fully connected layer are denoted as Conv, Deconv, BN, ReLU and FC respectively. The number under every block represents the channel number of Conv or Deconv. The array in bracket in every block indicates the kernel, stride and padding size of Conv or Deconv respectively.

In the tensor concatenation part, six feature maps extracted by the en-



coder from each channel are averaged to obtain the global features  $Feature_A$ ,  $Feature_B$  of  $I_A$  and  $I_B$ , respectively. Then,  $Feature_A$  and  $Feature_B$  are concatenated on the third channel.

In the decoder, the joint feature is upsampled and deconvolved through two transposed convolutional layers for size recovery and reconstruction. Finally, the single-channel focus map is output by a convolutional and activating layer.

**Discriminator  $D$ :** In the discriminator, eight convolutional layers are used to compress the input data continuously until the final sigmoid activation function is used to judge whether the input focus map is real or generated. Specifically, the input is a 7-channel tensor, i.e., the concatenation of source images and a focus map which is generated by  $G$  or be the real one from the training dataset. The kernel, padding and stride size of convolutional layers for down-sampling are set to guarantee the final output is a single element for judgment.

### 3.2. Loss Function

The objective function plays a crucial role in deep learning. Some works indicated that the original GAN suffers from training instability because during the  $D$  and  $G$  are trained to optimality alternately, the Jensen-Shannon divergence between the real data distribution  $\mathbb{P}_{data}$  and the noise distribution  $\mathbb{P}_z$  is minimized [36], which often leads to vanishing gradients. As a improved version, WGAN [38] is still subjected to either vanishing or exploding gradients without rational tuning of the clipping threshold  $c$  [39].

So in our work, we adopted the improved training of WGAN [39], the adversarial loss function of  $D$  and  $G$  are listed as equations (1) and (2):

$$\mathcal{L}_{adv}(D) = \mathbb{E}_{I_{A,B} \sim \mathbb{P}_{I_{A,B}}} [D(I_{A,B}, G(I_{A,B}))] - \mathbb{E}_{I_{A,B}, F \sim \mathbb{P}_{I_{A,B}, F}} [D(I_{A,B}, F)] \quad (1)$$

$$\mathcal{L}_{adv}(G) = -\mathbb{E}_{I_{A,B} \sim \mathbb{P}_{I_{A,B}}} [D(I_{A,B}, G(I_{A,B}))] \quad (2)$$

where  $I_{A,B}, F \sim \mathbb{P}_{I_{A,B}, F}$  in (1) denotes the inputs of  $D$  follow the joint distribution of the couple of images and focus maps from the real data.

As the main contribution in [39], the gradient penalty  $\mathcal{L}_{gp}$  is added into the loss of  $D$  to stabilize the training process and further improve the quality of

generated focus maps. That is:

$$\mathcal{L}_{gp} = \mathbb{E}_{I_{A,B}, \tilde{F} \sim \mathbb{P}_{I_{A,B}, \tilde{F}}} [(\|\nabla_{\tilde{F}} D(I_{A,B}, \tilde{F})\|_2 - 1)^2] \quad (3)$$

where  $\tilde{F}$  is sampled uniformly along a straight line between  $F$  and  $\hat{F}$ .

According to [34], compared with cross entropy loss used in FuseGAN, the loss function based on mean absolute value of error is more robust to the noise. Therefore, the  $\ell_1$ -norm is utilized as reconstruction loss  $\mathcal{L}_{rec}$  to measure the difference between the generated focus maps and the real ones, as shown in equation (4):

$$\mathcal{L}_{rec} = \mathbb{E}_{I_{A,B}, F \sim \mathbb{P}_{I_{A,B}, F}} [|F - G(I_{A,B})|] \quad (4)$$

So the total loss functions of MFIF-GAN can be defined by (5) and (6):

$$\min_D \mathcal{L}(D) = \mathcal{L}_{adv}(D) + \lambda_{gp} \mathcal{L}_{gp} \quad (5)$$

$$\min_G \mathcal{L}(G) = \mathcal{L}_{adv}(G) + \lambda_{rec} \mathcal{L}_{rec} \quad (6)$$

We use  $\lambda_{gp} = 10$  defaulted in [39] for all experiments. In order that  $\lambda_{gp}$  and  $\lambda_{rec}$  are used to adjust these two additional loss terms to the same level of importance, the value of  $\lambda_{rec}$  is set as same as  $\lambda_{gp}$ .

### 3.3. Post-processing in MFIF-GAN

The focus maps generated by  $G$  often suffer from misregistration or noise resulting in unsatisfactory fusion images. Therefore, we employ the small region removal (SRR) strategy for refinement. The SRR works on the binary matrix and it removes the region whose number of pixels is smaller than a threshold  $N$ . In this paper, we set  $N = 0.001WH$ , where  $W$  and  $H$  are the width and height of an image, respectively. The final focus maps  $\hat{F}_{final}$  can be obtained after this post-processing which is so simple and effective that it does not increase computational burden.

## 4. Experiments

In this section, the preparations of experiments including datasets, assessment metrics along with setting of training and testing are firstly introduced.

Based on three public test datasets, we compare our MFIF-GAN with eight representative SOTA methods, including spetial domain methods Quadtree [40]<sup>1</sup> and DSIFT [15]<sup>2</sup>, transform domain methods NSCT [6]<sup>3</sup>, CSR [41]<sup>4</sup> and MWGF [42]<sup>5</sup>, deep learning based methods MMF-Net [1]<sup>6</sup>, CNN [19]<sup>7</sup> and FuseGAN [11]<sup>8</sup>. Qualitative and quantitative results of all methods are provided in detail. In addition, the difficulty of avioding the DSE is analysed and a simple and effective solution is put forward. Subsequently, the edge diffusion and contraction experiments are proposed to verify the rationality of this solution. Finally, the ablation experiments are conducted to validate the contributions of several modules in our method.

#### 4.1. Experiments Setting

##### 4.1.1. Dataset

The MFIF training datasets which take the DSE into account are not available publicly. Therefore, we apply the  $\alpha$ -matte model [1] to the PASCAL VOC 2012 [24] to construct a synthetic training dataset with DSE which will be termed  $\alpha$ -matte dataset.

Each picture in this image segmentation database PASCAL VOC 2012 is accompanied by a segmentation map. We regard the binary segmentation map as a focus map  $F$  (matte  $\alpha^C$  in [1]). Using  $F$ , the clear foreground  $FG^C$  and background  $BG^C$  can be got as follows:

$$FG^C = F * I \quad (7)$$

$$BG^C = (1 - F) * I \quad (8)$$

---

<sup>1</sup><https://github.com/uzeful/Quadtree-Based-Multi-focus-Image-Fusion>

<sup>2</sup><http://www.escience.cn/people/liuyul/Codes.html>

<sup>3</sup><https://github.com/yuliu316316/MST-SR-Fusion-Toolbox>

<sup>4</sup><http://www.escience.cn/people/liuyul/Codes.html>

<sup>5</sup>[https://www.researchgate.net/publication/307415978\\_MATLAB\\_Code\\_of\\_Our\\_Multi-focus\\_Image\\_Fusion\\_Algorithm\\_MWGF](https://www.researchgate.net/publication/307415978_MATLAB_Code_of_Our_Multi-focus_Image_Fusion_Algorithm_MWGF)

Multi-focus\_Image\_Fusion\_Algorithm\_MWGF

<sup>6</sup><https://github.com/xytmhy/MMF-Net-Multi-Focus-Image-Fusion>

<sup>7</sup><http://home.ustc.edu.cn/~liuyul>

<sup>8</sup>The official codes of FuseGAN are unavailable, so we re-implement and re-train FuseGAN.

where  $*$  means pixel-wise production.

The blurred focus map  $F^B$  (matte  $\alpha^B$  in [1]) can be obtained by applying a gaussian filter  $G(x, y; \sigma)$  to corresponding  $F$ . That is:

$$F^B = G(x, y; \sigma) \otimes F \quad (9)$$

where  $\otimes$  represents the convolutional operator. The blurred foreground  $FG^B$  and background  $BG^B$  can be acquired in the same way.

Finally, according to the  $\alpha$ -matte model, a pair of training images  $I_A$  and  $I_B$  with only two valid surface (foreground surface  $S_{FG}$  and background surface  $S_{BG}$ ) can be obtained by equations (10) and (11) respectively.

$$\begin{aligned} I_A &= S_{FG}^{clear} + S_{BG}^{blurry} \\ &= FG^C + (1 - \alpha^C) * BG^B \\ &= F * I + (1 - F) * \{G(x, y; \sigma) \otimes [(1 - F) * I]\} \end{aligned} \quad (10)$$

$$\begin{aligned} I_B &= S_{FG}^{blurry} + S_{BG}^{clear} \\ &= FG^B + (1 - \alpha^B) * BG^C \\ &= G(x, y; \sigma) \otimes (F * I) + (1 - G(x, y; \sigma) \otimes F) * [(1 - F) * I] \end{aligned} \quad (11)$$

In order to verify the contribution of the  $\alpha$ -matte model, based on the generation method raised in [28], an another dataset without DSE is synthesized for the ablation experiment. In what follows, we call it conventional MFIF training dataset. In formula, the source images are obtained by (12) (13).

$$I_A = F * I + (1 - F) * (G(x, y; \sigma) \otimes I) \quad (12)$$

$$I_B = F * (G(x, y; \sigma) \otimes I) + (1 - F) * I \quad (13)$$

As for testing data, the famous Lytro [43] dataset is utilized. In addition, a new dataset called MFFW [5] which significantly suffers from the DSE is employed in the test. In order to verify the performance of our algorithm comprehensively, 10 pairs of gray images termed grayscale [13] is also used.

#### 4.1.2. Training and Testing Setup

In the training stage, we optimize  $G$  and  $D$  alternately. In order to better optimize the objective function and simplify the updating strategy of learning rate, we use the adam with two parameters  $\beta_1$  and  $\beta_2$  which are initialized to 0.5 and 0.999, respectively. And the linear declining strategy is used to update the learning rates of  $G$  and  $D$  both initialized to 0.0001. Besides, the update rate ratio between  $G$  and  $D$  is 1 : 5, which means that  $G$  is updated once after updating  $D$  for five times.

In the testing phase, we only retain  $G$  followed by a SRR to generate the focus maps  $\hat{F}$  and refine them. The processed focus maps  $\hat{F}_{final}$  are used to extract the clear regions and reconstruct the all-in-focus images as follows:

$$I_{fused} = I_A * \hat{F}_{final} + I_B * (1 - \hat{F}_{final}) \quad (14)$$

For the grayscale dataset, samples are tripled to form images with 3 channels as inputs of  $G$ .

#### 4.1.3. Quantitative Assessment Metrics

In order to evaluate the performance of different algorithms comprehensively, twelve objective metrics are utilized<sup>9</sup>, which are (1) information theory-based metrics including mutual information  $MI$  [44], Tsallis entropy based metric  $TE$  [45] and nonlinear correlation information entropy  $NCIE$  [46]; (2) image structure similarity-based metric: structure similarity index measure ( $SSIM$ ) based metric proposedal by Cui Yang et al. (also named Yang’s metric  $Q_Y$ ) [47]; (3) human perception inspired fusion metric: Chen-blum metric  $Q_{CB}$  [48] (4) image feature-based metrics including gradient-based metric  $Q_G$  [49], multiscale scheme based  $Q_M$  [50], spatial frequency based  $SF$  [51], linear index of fuzziness  $LIF$  [52], average gradient  $AG$ [53], mean square deviation  $MSD$  [26] and gray level difference  $GLD$  [26]. Detailed mathematical expressions of these metrics could be found in original papers or overview work [54].

---

<sup>9</sup>The implementation of these metrics are available at <https://github.com/zhengliu6699/imageFusionMetrics>

It is worth to note that the fused images are better if all metrics are larger except for *LIF*. These metrics have different emphases, so none of them is better than all others. The first eight traditional metrics (i.e. *MI*, *TE*, *NCIE*, *Q<sub>Y</sub>*, *Q<sub>CB</sub>*, *Q<sub>G</sub>*, *Q<sub>M</sub>* and *SF*) are widely used in assessment of images quality for their characteristics of computing agreements of fused images with the sources. Instead, the last four metrics (i.e. *LIF*, *AG*, *MSD* and *GLD*) are used to evaluate the performance of edge detail and contrast enhancement of the fused results in spite of the sources [26].

#### 4.2. Comparison with SOTA Methods

##### 4.2.1. Quantitative Comparison

Based on the above test datasets and evaluation metrics, the quantitative results with respect to the proposed MFIF-GAN and SOTAs are listed in Tab.1.

On the Lytro dataset, it can be clearly seen that on the first eight traditional metrics, our proposed MFIF-GAN trained on the  $\alpha$ -matte dataset is generally superior to other methods. Moreover, on the last four metrics which evaluate the edge quality, MFIF-GAN can still take the lead in addition to the MMF-Net which is specially designed and optimized for the DSE. On the MFFW, the absolute advantage of our MFIF-GAN compared with other SOTAs is obvious. As for the grayscale dataset, our method achieves comparable results to the Quadtree generally.

##### 4.2.2. Visual Comparison of Details

More attention could be paid to the details on the basis that the overall fusion results are good. So based on the 20th image in Lytro and the 11th in MFFW, the fusion results with detailed magnified of all methods, as shown in Fig.4, are compared visually to show the superior fusion performance of MFIF-GAN, especially in the region around the FDB.

Furthermore, by comparing the Fig.4(h) and 4(i), 4(q) and 4(r) respectively, it can be seen that if  $I_A$ , as the input of ConvCRFs in the FuseGAN, is replaced with  $I_B$  suffers from the DSE, the edge of the foreground will be much clearer.

Table 1: Average scores of fusion result based on Lytro, MFFW and grayscale datasets by all algorithms on 12 metrics. The best, the second best, and the third best results are highlighted in bold, double underlining, and underlining, respectively.

(a) Lytro									
	CNN	MMF-net	MWGF	Quadtree	DSIFT	CSR	NSCT	FuseGAN	MFIF-GAN
<i>MI</i>	<u>1.07075</u>	0.92506	1.01685	1.05303	<u>1.08438</u>	0.99020	0.90903	1.05501	<b>1.09446</b>
<i>TE</i>	<u>0.37853</u>	0.36443	0.37221	0.37658	<u>0.37925</u>	0.37288	0.36594	0.37610	<b>0.38034</b>
<i>NCIE</i>	<u>0.83933</u>	0.83067	0.83603	0.83806	<u>0.84021</u>	0.83400	0.82957	0.83896	<b>0.84097</b>
<i>Q<sub>G</sub></i>	0.70763	0.64492	<u>0.71059</u>	0.69854	0.70118	0.69508	0.68305	<u>0.70814</u>	<b>0.71786</b>
<i>Q<sub>M</sub></i>	<u>1.91707</u>	1.42079	1.73044	1.87318	<u>2.03527</u>	1.63746	1.40236	1.77586	<b>2.07952</b>
<i>SF</i>	-0.03422	<b>-0.00845</b>	-0.03875	-0.02546	<u>-0.02442</u>	-0.03371	-0.03258	-0.03629	<u>-0.02324</u>
<i>Q<sub>Y</sub></i>	<u>0.97583</u>	0.94947	0.97004	0.973990	<u>0.97615</u>	0.95141	0.9533	0.97419	<b>0.97696</b>
<i>Q<sub>CB</sub></i>	<u>0.79612</u>	0.74312	0.77483	0.78761	<b>0.79886</b>	0.76064	0.74455	0.784	<u>0.79764</u>
<i>LIF</i>	0.38740	<b>0.38670</b>	0.387790	0.38714	<u>0.38694</u>	0.38737	0.38959	0.38823	<u>0.38698</u>
<i>AG</i>	2.99603	<b>3.09201</b>	2.97081	3.02048	<u>3.02212</u>	2.97995	3.00927	3.00098	<u>3.0266</u>
<i>MSD</i>	0.07007	<b>0.07059</b>	0.07000	0.070130	<u>0.07017</u>	0.07001	0.07003	0.06999	<u>0.07019</u>
<i>GLD</i>	14.75660	<b>15.23405</b>	14.62293	14.87703	<u>14.88406</u>	14.67629	14.82605	14.77889	<u>14.90642</u>

(b) MFFW								
	CNN	MWGF	Quadtree	DSIFT	CSR	NSCT	FuseGAN	MFIF-GAN
<i>MI</i>	0.99738	0.96529	<u>1.02036</u>	0.98671	0.8907	0.78236	<u>1.01877</u>	<b>1.06806</b>
<i>TE</i>	0.364	0.35761	<u>0.36466</u>	0.35911	0.3475	0.34291	<u>0.36908</u>	<b>0.37169</b>
<i>NCIE</i>	0.83288	0.83086	<u>0.83451</u>	0.83298	0.8271	0.82123	<u>0.83531</u>	<b>0.83716</b>
<i>Q<sub>G</sub></i>	0.56866	<u>0.60566</u>	0.49265	<b>0.63777</b>	0.53382	0.56998	<u>0.62866</u>	0.56345
<i>Q<sub>M</sub></i>	1.94031	1.8218	<u>2.08961</u>	<u>2.03046</u>	1.88064	1.14658	1.83548	<b>2.21075</b>
<i>SF</i>	-0.05251	-0.05472	-0.04142	<u>-0.03498</u>	<u>-0.03717</u>	-0.04652	-0.04685	<b>-0.03111</b>
<i>Q<sub>Y</sub></i>	0.96754	<u>0.97207</u>	0.96834	0.93459	0.86835	0.91066	<u>0.97554</u>	<b>0.97939</b>
<i>Q<sub>CB</sub></i>	0.74025	0.74085	<u>0.75113</u>	0.72927	0.69403	0.67343	<u>0.74159</u>	<b>0.75624</b>
<i>LIF</i>	0.38654	0.38852	<u>0.38617</u>	0.38884	0.38709	0.38626	<u>0.38522</u>	<b>0.38361</b>
<i>AG</i>	3.53508	3.51182	3.60422	<u>3.62413</u>	<b>3.63075</b>	3.59994	3.55498	<u>3.62057</u>
<i>MSD</i>	<b>0.07931</b>	0.07833	0.07857	0.07846	0.07843	<u>0.07922</u>	0.07879	<u>0.07902</u>
<i>GLD</i>	17.49452	17.36662	17.83513	<u>17.92287</u>	<b>17.95869</b>	17.80467	17.59685	<u>17.91793</u>

(c) grayscale								
	CNN	MWGF	Quadtree	DSIFT	CSR	NSCT	FuseGAN	MFIF-GAN
<i>MI</i>	1.1222	1.10868	<b>1.15406</b>	<u>1.14503</u>	1.04652	0.85708	1.07939	<u>1.13731</u>
<i>TE</i>	0.41359	0.41237	<u>0.41746</u>	<u>0.41653</u>	0.41127	0.38899	0.41031	<b>0.41859</b>
<i>NCIE</i>	0.8376	0.83731	<b>0.83957</b>	<u>0.83889</u>	0.83307	0.82378	0.83649	<u>0.83899</u>
<i>Q<sub>G</sub></i>	0.67711	<u>0.67974</u>	0.63484	<u>0.68076</u>	0.67628	0.63163	0.61953	<b>0.68343</b>
<i>Q<sub>M</sub></i>	2.33876	2.32259	<b>2.46421</b>	<u>2.44523</u>	2.22342	1.55645	1.73248	<u>2.3914</u>
<i>SF</i>	-0.0414	-0.04321	<u>-0.03422</u>	-0.0353	-0.03964	-0.03928	<b>0.02467</b>	<u>-0.03342</u>
<i>Q<sub>Y</sub></i>	<u>0.97724</u>	<u>0.97809</u>	<b>0.97873</b>	0.97517	0.93837	0.93601	0.95378	0.97348
<i>Q<sub>CB</sub></i>	<u>0.76327</u>	<b>0.76461</b>	0.76313	<u>0.76427</u>	0.72702	0.7029	0.74415	0.7558
<i>LIF</i>	0.47571	0.47552	<u>0.47551</u>	0.47556	0.47578	<u>0.47465</u>	0.49394	<b>0.47458</b>
<i>AG</i>	3.53597	3.53821	<u>3.56883</u>	<u>3.5687</u>	3.52606	<b>3.58797</b>	3.54217	<u>3.56084</u>
<i>MSD</i>	0.13997	0.13984	0.14002	0.14009	0.13987	<u>0.14014</u>	<b>0.15071</b>	<u>0.14064</u>
<i>GLD</i>	17.15701	17.1702	<u>17.31683</u>	<u>17.31368</u>	17.10948	<b>17.42544</b>	17.1133	<u>17.27329</u>

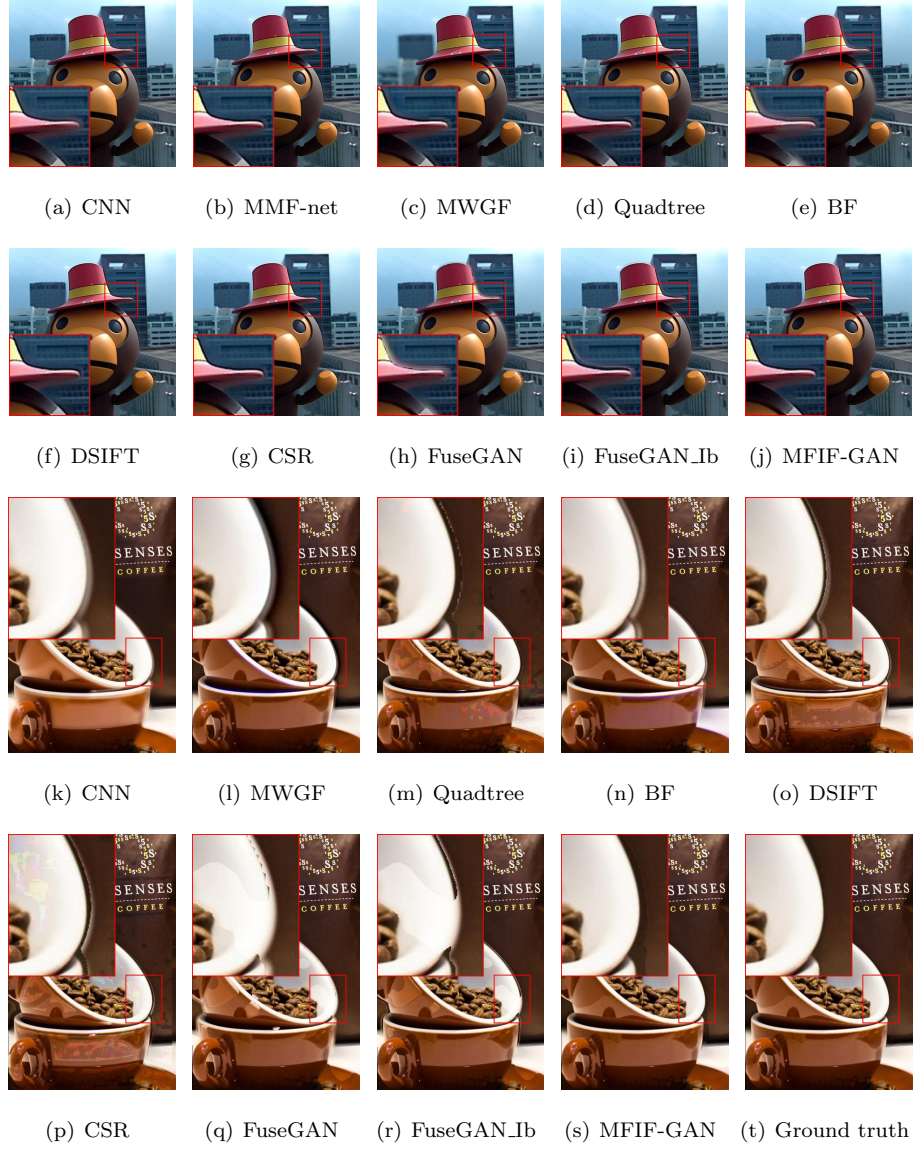


Figure 4: The fusion results on Lytro (20th) and MFFW (11th) with detail magnified of all algorithms. The FuseGAN\_Ib exhibits the fusion result by FuseGAN with ConvCRF which feed with  $I_B$  as ground truth.



#### 4.2.3. Solution to mitigating the DSE

As we discussed in the drawbacks of FuseGAN, when the all-in-focus image do not exist, the  $I_A$  has to be used as ground truth for the ConvCRFs. However, the DSE vanishes when it comes to  $I_A$ , which means the FDB in  $I_A$  is definitely clear. Thus the outputs of FuseGAN are focus maps which represent the real foreground objects with sharp edges. According to the  $\alpha$ -matte model theory and the experience in daily observation, using these focus maps could result in two completely different situations in the procedure of extracting clear regions from source images:

When  $I_A$  is processed, the extracted foreground region is ideal. In contrast, when it comes to  $I_B$ , because of the existence of the DSE, there must be a part of the foreground information diffuses into the background. So the diffusion laying outside the foreground objects remain in the clear background (as shown obviously in the Fig.4(h) and 4(q)). Consequently, the fuzzy FDB appears in the fusion images, which is the diffusion of the foreground in  $I_B$  essentially. That also partially explains why the undesirable results can be alleviated to some extent in FuseGAN when  $I_A$  is substituted with  $I_B$ , as shown in Fig.4(i) and 4(r).

Actually, a part of the information about clear backgrounds is indeed missed as it is covered by the diffusion of foregrounds in  $I_B$ . Moreover, these regions are irregular, as the width is affected by the shape of foregrounds and the distance from different positions to the sensor. So it is extremely complex and nontrivial to ideally handle FDB regions and eliminate the DSE.

One of the solutions is to generate focus maps in which the foregrounds are mildly larger than real objects. Using these focus maps can remain the backgrounds information around foregrounds in  $I_A$ . Actually, focus maps obtained by MFIF-GAN is exactly what we expected.

To illustrate this statement, we make the difference between two sets of focus maps generated by baseline FuseGAN and MFIF-GAN respectively. As shown in Fig.5(c), the appearance of white edges indicates this statement obviously.

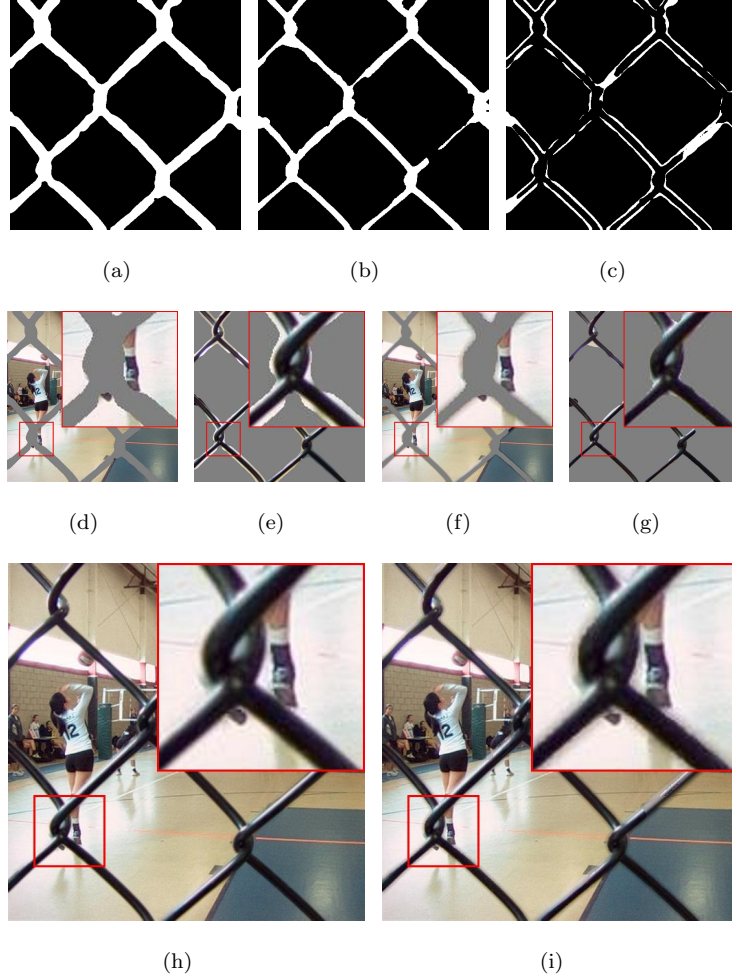


Figure 5: (a) and (b) exhibits the  $\hat{F}_{final}$  generated by MFIF-GAN and FuseGAN respectively; (c) is the difference between two focus maps; (d) and (e) shows the background and foreground extracted respectively by  $\hat{F}_{final}$  in (a); (f) and (g) are the counterparts processed by  $\hat{F}_{final}$  in (b); (h) and (i) are fusion results of MFIF-GAN and FuseGAN with detail magnified.

To show the improvement brought by this characteristic more clearly and intuitively, we used these two focus maps respectively to extract the foreground and background of source images. As shown in Fig.5(d) and 5(e), the background extracted by the focus map generated by MFIF-GAN partially eliminates the edge diffusion, that is DSE. Meanwhile the extracted foreground con-

tains part of the blurred background which can smooth the FDB. In contrast, as shown clearly in Fig.5(f) and 5(g), even though the foreground extracted by the focus map generated by FuseGAN seems to be ideal, the extracted background in Fig.5(f) retains foreground diffusion around the edge.

#### 4.2.4. Diffusion and Contraction Experiments

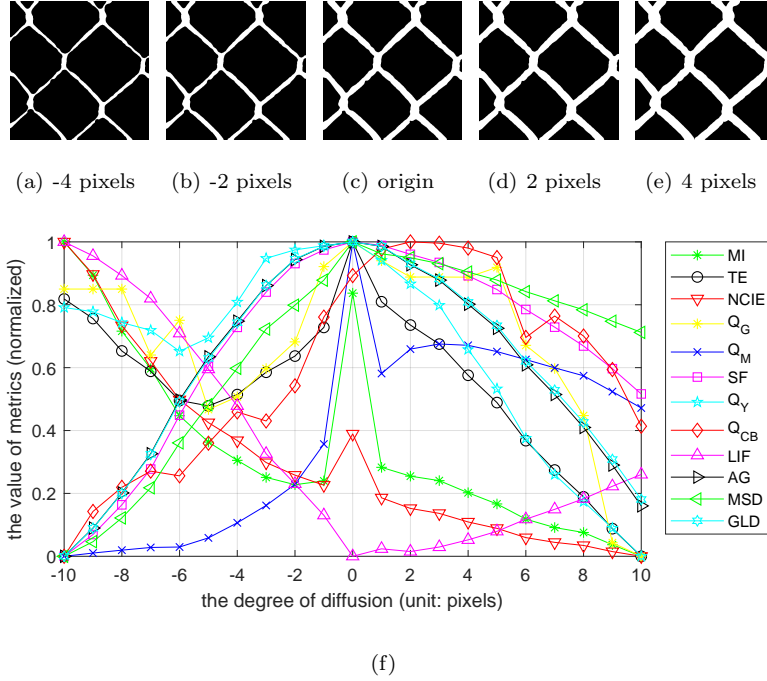


Figure 6: (a)-(e) are focus maps with different degree of edge diffusion or contraction in which (c) is the original focus map generated by our method. And (f) is the average performance on Lytro using these focus maps. All values of each metrics are normalized to  $[0-1]$ .

The scale of the foreground in focus maps is crucial when we employ proposed solution to attenuate the DSE. In order to explore the rational size of the foreground regions and confirm the effectiveness of MFIF-GAN, we design a diffusion and contraction module to enlarge or shrink the foreground area in focus maps generated by our method at the pixel level. As shown in Fig.6 (a)-(e), the negative value of the degree of diffusion indicates foreground regions

are contracted by certain pixels. According to equation (14), a series of focus maps with different degree of edge diffusion or contraction are used as guidance to fuse source images.

As reported in Fig.6(f), the results assessed by  $MI$  and  $NCIE$  indicate that apart from using original focus maps, the performances decrease with the expansion of the foreground regions. And the line of  $Q_{CB}$  shows that the foreground regions which are two pixels larger than the original ones could bring best performance. Except for these three metrics, experimental results generally illustrate that using the focus maps without any operations achieves the largest values. That demonstrates MFIF-GAN can produce focus maps which have accurate size of foreground regions and attenuate the DSE exactly at the pixel level.

#### 4.2.5. Execution Time

This section is about the comparison of computational efficiency. Tab.2 lists the mean execution time of each method on testing datasets<sup>10</sup>. The experiments are carried out on a computer with Intel Core i7-10700K CPU @ 3.8GHz and RTX 2080ti GPU. The results indicate that compared with SOTAs, the fusion efficiency of our algorithm is the highest.

Table 2: Average used time of all methods for pre-pair images fusion (unit: seconds)

	CNN	MWGF	Quadtree	DSIFT	CSR	NSCT	FuseGAN	MFIF-GAN
Lytro	25.6188	1.9677	0.5416	0.9095	120.9291	1.7989	0.4976	<b>0.2229</b>
MFFW	28.6874	2.2521	0.4922	1.6303	139.3664	2.2881	0.5019	<b>0.2236</b>
grayscale	18.0621	0.4808	0.3029	0.7909	28.9021	0.4929	0.2883	<b>0.1344</b>

FuseGAN needs extra post-processing, so we record the time with respect to the generation of initial focus maps, post-processing and final fusion. The average time used are (Lytro) 0.2135s, 0.2355s, 0.0486s; (MFFW) 0.2156s, 0.2393s,

<sup>10</sup>Because the fusion results of MMF-net on Lytro are used directly, this method is not involved in the comparison.

0.047s; (grayscale) 0.078s, 0.1969s, 0.0133s respectively.

### 4.3. Ablation Experiments

The innovations of our MFIF-GAN include a new encoder with six parallel branches as well as attention modules, the well-designed loss function with gradient regularization and  $\ell_1$ -norm based reconstruction, and a simple but effective post-processing strategy. In addition, the network is trained on an  $\alpha$ -matte dataset. To validate the role of each element in our work, a series of ablation experiments are conducted here. The results are shown in Fig.7.

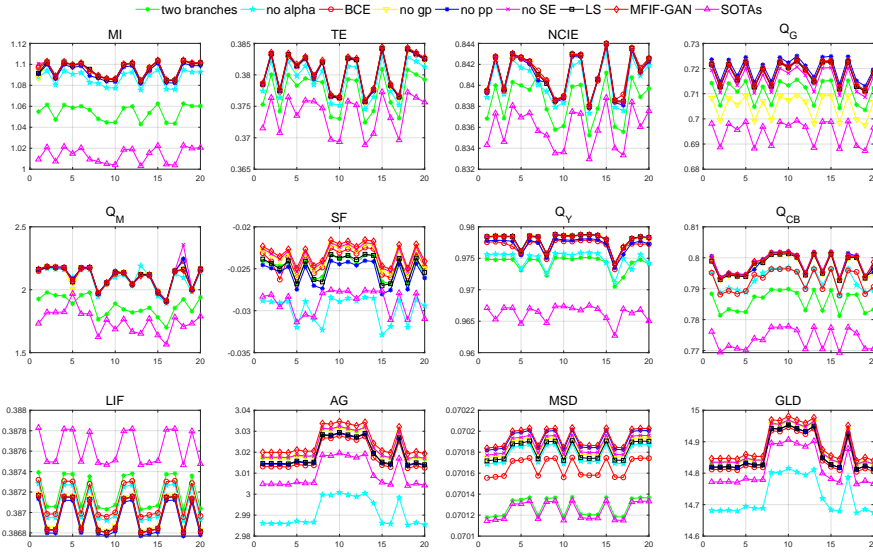


Figure 7: Score lines of ablation experiments based on Lytro with regard to each metric. The lines named “SOTAs” are average scores in terms of all SOTAs on every image.

(1) In order to verify the capability of our MFIF-GAN to extract features of color images, the structure of encoder in generator are redesigned with two parallel sub-networks which input images with single channel. (2) To show the effectiveness of the  $\alpha$ -matte model, our network is also trained on the conventional MFIF dataset generated in section 4.1.1. From score lines named “two branches” and “no alpha” as shown in every sub-figure, we can see that apart from the SOTAs, the network with two branches and MFIF-GAN trained

on conventional MFIF dataset are generally inferior to all other counterparts in ablation experiments, which indicates that the structure of the network and training data play significant roles and more implicit features could be extracted in color images suffering from the DSE.

(3) The  $\ell_1$ -norm based reconstruction loss  $\mathcal{L}_{rec}$  (equation (4)) is substituted by the BCE used in baseline work to testify the validity of this loss. Compared with other sub-figures, the worse performances of line “BCE” on edge detail assessment metrics ( $LIF$ ,  $AG$ ,  $MSD$  and  $GLD$ ) indicate that the  $\ell_1$ -norm based loss  $\mathcal{L}_{rec}$  could force the generator to pay more attention to the information around the FDB and enhance the edge details.

(4) The gradient penalty  $\mathcal{L}_{gp}$  (equation (3)), and post-processing procedure are removed respectively in MFIF-GAN. Also, the SE-ResNet block is replaced by general ResNet to prove the improvement brought by this attention mechanism. In addition, to show the role of adversarial loss  $\mathcal{L}_{adv}$  (equations (1) and (2)) risen in [39], they are replaced by the least squares loss [32] used in the FuseGAN. The lines named “no gp”, “no pp”, “no SE” and “LS” show that each of these factors improves the performance of fusion results to some extent, but generally none of them is more important than others.

Last but not least, as shown in score lines “SOTAs”, it is worthy to note that without any one of factors, our algorithm still has a big advantage over other SOTAs generally, which indicates that proposed MFIF-GAN with a new architecture and well-designed loss function has strong robustness for gradient regularization, post-processing, attention mechanism and training dataset.

## 5. Conclusions

In this paper, we propose a generative adversarial network termed MFIF-GAN for the MFIF task and put forward a new solution to attenuate the DSE which is rampant in this field. The motivation of our work is to guarantee the foreground regions in generated focus maps are mildly larger than the corresponding objects, which can simulate the DSE and further exactly alleviate this

annoying effect. The innovation is that attention mechanism is exploited in the network which has a new architecture with six branches to extract features. And the  $\ell_1$ -norm reconstruction loss and gradient penalty is creatively added to the optimization function to enhance the edge details and improve the quality of the outputs. Moreover, the SRR algorithm for post-processing is used to refine the initial focus maps in a computational effective way. Last but not least, based on a synthetic  $\alpha$ -matte training dataset, this novel end-to-end color multi-focus image fusion algorithm can fuse more realistic images especially around the FDB.

As a new fusion algorithm, experiments demonstrate that our MFIF-GAN is superior to other representative SOTA methods on visual perception, quantitative analysis and efficiency. The edge diffusion and contraction module proves that following the proposed solution, MFIF-GAN can generate accurate focus maps and alleviate the DSE at the pixel level, which can bring more satisfactory pretreatment to other computer vision tasks.

## Acknowledgements

The research is supported by the National Key Research and Development Program of China under grant 2018AAA0102201, the National Natural Science Foundation of China under grant 61877049, 61976174 and 11671317.

## References

- [1] H. Ma, Q. Liao, J. Zhang, S. Liu, J.-H. Xue, An  $\alpha$ -matte boundary defocus model-based cascaded network for multi-focus image fusion, *IEEE Transactions on Image Processing* 29 (2020) 8668–8679.
- [2] A. A. Goshtasby, S. Nikolov, Image fusion: advances in the state of the art, *Information fusion* 2 (8) (2007) 114–118.
- [3] I. De, B. Chanda, B. Chattopadhyay, Enhancing effective depth-of-field by image fusion using mathematical morphology, *Image and Vision Computing* 24 (12) (2006) 1278–1287.

- [4] T. Stathaki, *Image Fusion: Algorithms and Applications*, Elsevier, 2011.
- [5] S. Xu, X. Wei, C. Zhang, J. Liu, J. Zhang, Mffw: A new dataset for multi-focus image fusion, *arXiv preprint arXiv:2002.04780*.
- [6] Q. Zhang, B.-l. Guo, Multifocus image fusion using the nonsubsampling contourlet transform, *Signal processing* 89 (7) (2009) 1334–1346.
- [7] A. L. da Cunha, J. Zhou, M. N. Do, The nonsubsampling contourlet transform: Theory, design, and applications, *IEEE Trans. Image Processing* 15 (10) (2006) 3089–3101.
- [8] B. Yang, S. Li, Multifocus image fusion and restoration with sparse representation, *IEEE Transactions on Instrumentation and Measurement* 59 (4) (2009) 884–892.
- [9] Q. Zhang, M. D. Levine, Robust multi-focus image fusion using multi-task sparse representation and spatial context, *IEEE Transactions on Image Processing* 25 (5) (2016) 2045–2058.
- [10] Y. Liu, S. Liu, Z. Wang, A general framework for image fusion based on multi-scale transform and sparse representation, *Information Fusion* 24 (2015) 147–164.
- [11] X. Guo, R. Nie, J. Cao, D. Zhou, L. Mei, K. He, Fusegan: Learning to fuse multi-focus image via conditional generative adversarial network, *IEEE Trans. Multimedia* 21 (8) (2019) 1982–1996.
- [12] X. Zhang, X. Li, Z. Liu, Y. Feng, Multi-focus image fusion using image-partition-based focus detection, *Signal Processing* 102 (2014) 64–76.
- [13] Y. Liu, L. Wang, J. Cheng, C. Li, X. Chen, Multi-focus image fusion: A survey of the state of the art, *Information Fusion* 64 (2020) 71–91.
- [14] S. Li, J. T. Kwok, Y. Wang, Combination of images with diverse focuses using the spatial frequency, *Information fusion* 2 (3) (2001) 169–176.



- [15] Y. Liu, S. Liu, Z. Wang, Multi-focus image fusion with dense SIFT, *Information Fusion* 23 (2015) 139–155.
- [16] I. De, B. Chanda, Multi-focus image fusion using a morphology-based focus measure in a quad-tree structure, *Information Fusion* 14 (2) (2013) 136–146.
- [17] M. Li, W. Cai, Z. Tan, A region-based multi-sensor image fusion scheme using pulse-coupled neural network, *Pattern Recognition Letters* 27 (16) (2006) 1948–1956.
- [18] Y. Zhang, X. Bai, T. Wang, Boundary finding based multi-focus image fusion through multi-scale morphological focus-measure, *Information Fusion* 35 (2017) 81–101.
- [19] Y. Liu, X. Chen, H. Peng, Z. Wang, Multi-focus image fusion with a deep convolutional neural network, *Information Fusion* 36 (2017) 191–207.
- [20] R. Guo, X.-j. Shen, X.-y. Dong, X.-l. Zhang, Multi-focus image fusion based on fully convolutional networks, *Frontiers of Information Technology & Electronic Engineering* 21 (7) (2020) 1019–1033.
- [21] H. Ma, J. Zhang, S. Liu, Q. Liao, Boundary aware multi-focus image fusion using deep neural network, in: *2019 IEEE International Conference on Multimedia and Expo (ICME)*, IEEE, 2019, pp. 1150–1155.
- [22] C. Du, S. Gao, Image segmentation-based multi-focus image fusion through multi-scale convolutional neural network, *IEEE Access* 5 (2017) 15750–15761.
- [23] J. Hu, L. Shen, G. Sun, Squeeze-and-excitation networks, in: *Proceedings of the IEEE Conference on Computer Vision and Pattern Recognition (CVPR)*, 2018, pp. 7132–7141.
- [24] M. Everingham, S. A. Eslami, L. Van Gool, C. K. Williams, J. Winn, A. Zisserman, The pascal visual object classes challenge: A retrospective, *International Journal of Computer Vision* 111 (1) (2015) 98–136.

- [25] Y. Liu, X. Chen, Z. Wang, Z. J. Wang, R. K. Ward, X. Wang, Deep learning for pixel-level image fusion: Recent advances and future prospects, *Information Fusion* 42 (2018) 158–173.
- [26] W. Zhao, D. Wang, H. Lu, Multi-focus image fusion with a natural enhancement via a joint multi-level deeply supervised convolutional neural network, *IEEE Transactions on Circuits and Systems for Video Technology* 29 (4) (2018) 1102–1115.
- [27] B. Ma, X. Ban, H. Huang, Y. Zhu, Sef-fuse: An unsupervised deep model for multi-focus image fusion, *CoRR* abs/1908.01703. [arXiv:1908.01703](#).
- [28] F. A. Guerrero-Peña, P. D. Marrero-Fernández, T. I. Ren, G. C. Vasconcelos, A. Cunha, A multiple source hourglass deep network for multi-focus image fusion, *CoRR* abs/1908.10945. [arXiv:1908.10945](#).
- [29] K. He, X. Zhang, S. Ren, J. Sun, Deep residual learning for image recognition, in: *Proceedings of the IEEE conference on computer vision and pattern recognition*, 2016, pp. 770–778.
- [30] C. Szegedy, W. Liu, Y. Jia, P. Sermanet, S. Reed, D. Anguelov, D. Erhan, V. Vanhoucke, A. Rabinovich, Going deeper with convolutions, in: *Proceedings of the IEEE conference on computer vision and pattern recognition*, 2015, pp. 1–9.
- [31] M. Mirza, S. Osindero, Conditional generative adversarial nets, *arXiv preprint arXiv:1411.1784*.
- [32] X. Mao, Q. Li, H. Xie, R. Y. Lau, Z. Wang, S. Paul Smolley, Least squares generative adversarial networks, in: *Proceedings of the IEEE International Conference on Computer Vision*, 2017, pp. 2794–2802.
- [33] Z. Huang, W. Xu, K. Yu, Bidirectional lstm-crf models for sequence tagging, *arXiv preprint arXiv:1508.01991*.

- [34] A. Ghosh, H. Kumar, P. Sastry, Robust loss functions under label noise for deep neural networks, arXiv preprint arXiv:1712.09482.
- [35] H. Zhang, Z. Le, Z. Shao, H. Xu, J. Ma, Mff-gan: An unsupervised generative adversarial network with adaptive and gradient joint constraints for multi-focus image fusion, *Information Fusion* 66 (2020) 40–53.
- [36] I. Goodfellow, J. Pouget-Abadie, M. Mirza, B. Xu, D. Warde-Farley, S. Ozair, A. Courville, Y. Bengio, Generative adversarial nets, in: *Advances in neural information processing systems*, 2014, pp. 2672–2680.
- [37] S. Ioffe, C. Szegedy, Batch normalization: Accelerating deep network training by reducing internal covariate shift, arXiv preprint arXiv:1502.03167.
- [38] M. Arjovsky, S. Chintala, L. Bottou, Wasserstein gan, arXiv preprint arXiv:1701.07875.
- [39] I. Gulrajani, F. Ahmed, M. Arjovsky, V. Dumoulin, A. C. Courville, Improved training of wasserstein gans, in: *Advances in neural information processing systems*, 2017, pp. 5767–5777.
- [40] X. Bai, Y. Zhang, F. Zhou, B. Xue, Quadtree-based multi-focus image fusion using a weighted focus-measure, *Information Fusion* 22 (2015) 105–118.
- [41] Y. Liu, X. Chen, R. K. Ward, Z. J. Wang, Image fusion with convolutional sparse representation, *IEEE Signal Process. Lett.* 23 (12) (2016) 1882–1886.
- [42] Z. Zhou, S. Li, B. Wang, Multi-scale weighted gradient-based fusion for multi-focus images, *Information Fusion* 20 (2014) 60–72.
- [43] M. Nejati, S. Samavi, S. Shirani, Multi-focus image fusion using dictionary-based sparse representation, *Information Fusion* 25 (2015) 72–84.
- [44] Guihong Qu, Dali Zhang, Pingfan Yan, Information measure for performance of image fusion, *Electronics Letters* 38 (7) (2002) 313–315.

- [45] N. Cvejic, C. N. Canagarajah, D. R. Bull, Image fusion metric based on mutual information and tsallis entropy, *Electronics Letters* 42 (11) (2006) 626–627.
- [46] T. Stathaki, *Image Fusion: algorithms and applications*, Elsevier, 2011.
- [47] C. Yang, J. Zhang, X. Wang, X. Liu, A novel similarity based quality metric for image fusion, *Information Fusion* 9 (2) (2008) 156–160.
- [48] Y. Chen, R. S. Blum, A new automated quality assessment algorithm for image fusion, *Image Vision Comput.* 27 (10) (2009) 1421–1432.
- [49] C. Xydeas, , V. Petrovic, Objective image fusion performance measure, *Electronics letters* 36 (4) (2000) 308–309.
- [50] P.-w. Wang, B. Liu, A novel image fusion metric based on multi-scale analysis, in: *2008 9th International Conference on Signal Processing, IEEE*, 2008, pp. 965–968.
- [51] Y. Zheng, E. A. Essock, B. C. Hansen, A. M. Haun, A new metric based on extended spatial frequency and its application to DWT based fusion algorithms, *Information Fusion* 8 (2) (2007) 177–192.
- [52] X. Bai, F. Zhou, B. Xue, Noise-suppressed image enhancement using multiscale top-hat selection transform through region extraction, *Appl. Opt.* 51 (3) (2012) 338–347.
- [53] G. Cui, H. Feng, Z. Xu, Q. Li, Y. Chen, Detail preserved fusion of visible and infrared images using regional saliency extraction and multi-scale image decomposition, *Optics Communications* 341 (2015) 199 – 209.
- [54] Z. Liu, E. Blasch, Z. Xue, J. Zhao, R. Laganière, W. Wu, Objective assessment of multiresolution image fusion algorithms for context enhancement in night vision: A comparative study, *IEEE Trans. Pattern Anal. Mach. Intell.* 34 (1) (2012) 94–109.